Thermal Analysis of InP Lasers Transfer Printed to Silicon Photonics Substrates

Ruggero Loi, James O'Callaghan, Brendan Roycroft, Zhiheng Quan, Kevin Thomas, Agnieszka Gocalinska, Emanuele Pelucchi, Antonio Jose Trindade, Christopher Anthony Bower, and Brian Corbett

***Abstract*—The thermal performance of Fabry–Perot InP lasers integrated onto different silicon photonics substrates by micro-transfer printing is assessed. 500-μm-long ridge waveguide lasers on the original 350-μm-thick InP have an experimental thermal impedance, Z_{EXP}, of 57 K/W that is reduced to 38 K/W after printing to a 500-μm-thick Si substrate. Z_{EXP} for lasers printed on silicon-on-insulator wafers is ∼94 K/W, which is more than two times higher than that of the laser printed on the Si substrate. Z_{EXP} of lasers printed on thermally insulating layers like benzocyclobutene (BCB) or SiO_2 increases with the thickness of the layer. BCB adhesive layers as thin as 50 nm limit Z_{EXP} to be greater than 55 K/W. The thermal properties for the different situations were modeled using finite-element simulations which confirmed the experimental results within 10% accuracy. The simulations show how changes in the geometry and the materials of the integration platform can influence the resulting thermal impedance.**

***Index Terms*—Heterogeneous integration, III–V semiconductor laser, silicon photonics, thermal management.**

I. Introduction

THE interest in silicon photonics has grown quickly in the last decade because of the possibility to use the high-volume manufacturing of the CMOS microelectronics industry [1], [2] for low-cost photonic circuits. The preferred Silicon-on-Insulator (SOI) platform of 220 nm of Si on 2 μm of SiO_2 on a silicon substrate offers compact waveguides thanks to the high refractive index contrast between the silicon waveguide core and the cladding. The need for integrating active photonic devices on SOI has been successfully accomplished by die/wafer bonding [3]–[8] and more recently by micro-transfer-printing (μTP) [9]–[11]. In particular, InP-based Fabry-Perot and DFB lasers, LEDs, and photodiodes have been heterogeneously integrated with silicon photonics by using μTP [12]–[15]. There is growing interest in μTP due to its placement accuracy combined with high-throughput parallel transfer [16]–[18]. With μTP, devices can be pre-fabricated completely in high dense arrays before transfer, improving material usage and enabling known-good-die methods. Arrays of III-V material structures of the desired dimensions can be also transfer-printed and post-processed after their attachment onto the new platform. μTP allows for integration onto both rigid and flexible substrates with and without adhesive layers [19], [20].

Thermal issues can be critical for lasers operating on silicon photonics [21]. The heat generated by an integrated laser will increase the temperature of the active region shifting its wavelength and reducing its efficiency. The heat will also affect the platform on which the device operates through, for example, the resultant temperature distribution changing the properties of many devices (e.g., ring resonators, phase modulators) through the temperature dependence of the refractive index of silicon. In fact, while silicon is an excellent thermal conductor with thermal conductivity, σ_{Si} ∼130 $\mathrm{Wm^{-1}K^{-1}}$, the buried oxide in the SOI has poor thermal conductivity of σ_{SiO2} ∼1.4 $\mathrm{Wm^{-1}K^{-1}}$. Since this represents an issue for the operation of the active devices on the SOI, the integration of III-V lasers requires careful attention of the system geometry and the materials involved to manage the heat produced [22]–[24]. In the die bonding approach the heat should be dissipated through the buried oxide layer, so thermal shunts, metallic vias and trenches have been applied to sink the heat from the device to the Si substrate along preferential paths [24]–[26]. This approach involves a high level of complexity in fabrication, especially after the integration of the III-V to the SOI. In particular, in the case of evanescent coupling the use of thermal shunts is limited by the width of the die and the interaction with the light in the SOI waveguide. Another possibility consists in bonding the III-V laser die upside down on a metal sub-mount in contact with the Si substrate while achieving light coupling to the SOI waveguide by gratings [4], [27]. A different approach is to sink the heat to the substrate by μTP of the devices inside a trench on the SOI directly on the silicon substrate and then edge coupling the light to the waveguides [28], [29].

In this work, we present experimental data and thermal analysis (Section III) of InP lasers heterogeneously integrated to different substrates by μTP. In particular, we compare the thermal impedance of lasers directly printed on SOI and on a Si substrate. We also investigate the influence of different intermediate layers between the transferred laser and the substrate on

Manuscript received August 20, 2018; revised October 26, 2018; accepted November 8, 2018. Date of publication November 13, 2018; date of current version November 29, 2018. This work was supported in part by Science Foundation Ireland under Grants 12/RC/2276 (IPIC) and 15/IA/2864, and in part by the European Union's Horizon 2020 Research and Innovation Programme under Grant 645314 (TOP-HIT). *(Corresponding author: Ruggero Loi.)*

R. Loi, J. O'Callaghan, B. Roycroft, Z. Quan, K. Thomas, A. Gocalinska, E. Pelucchi, and B. Corbett are with the Tyndall National Institute, University College Cork, Cork T12R5CP, Ireland (e-mail: ruggero.loi@tyndall.ie; james.ocallaghan@tyndall.ie; brendan.roycroft@tyndall.ie; zhiheng.quan@tyndall.ie; kevin.thomas@tyndall.ie; agnieszka.gocalinska@tyndall.ie; emanuele.pelucchi@tyndall.ie; brian.corbett@tyndall.ie).

A. J. Trindade and C. A. Bower are with X-Celeprint Limited, Cork T12R5CP, Ireland (e-mail: ajosetrindade@x-celeprint.com; cbower@x-celeprint.com).

Color versions of one or more of the figures in this paper are available online at http://ieeexplore.ieee.org.

Digital Object Identifier 10.1109/JLT.2018.2881179

the thermal impedance. In Section IV we compare the measured thermal impedance with simulations and show how changes in the geometry and the materials of the system can influence the thermal impedance.

II. Experimental

A. Laser Devices

The metal-organic vapor phase epitaxy (MOVPE) grown layer structure of the laser is as used in our previous work [30]. A 6 quantum well active region is embedded in a step index waveguide of 336 nm total thickness. The waveguide is clad by 1.5-μm-thick n- and p- doped InP, a cap layer of p-doped InGaAs allows electrical contacting on the p-side. The bottom of the active region is 1615 nm from the 500-nm-thick InAlAs sacrificial layer which is included between the substrate and the n-InP cladding layer of the laser allowing for the release of the devices from the native InP wafer. The mode overlap is 6.6% with the quantum wells. The transverse mode reaches 0.5 μm into the InP cladding layers making the mode independent of the contact layer or the substrate. This epitaxial structure is suitable for edge coupling to a silicon or other waveguide.

The micro-transfer-printable lasers are completely pre-fabricated on the source InP wafer as dense arrays (about 1,000 devices per cm^2) of 550 μm long and 60 μm or 80 μm wide coupons and are aligned along the major flat of the wafer. A 500 μm long laser cavity has a high reflection coated facet (metal mirror) and an emitting facet passivated by an optically neutral SiO_2 layer. A 2.5 μm wide ridge etched just above the active region confines the light laterally. The fabrication of the lasers includes the steps for preparing the coupons to the undercut and the μTP [12], [30]. The devices are encapsulated with a passivation layer in order to protect the III-V material during the undercut. A resist tethering system restrains the coupons to the InP substrate holding them in place during the undercut [see Fig. 1a]. The coupons are released from their native substrate by selectively etching the InAlAs sacrificial layer in $FeCl_3$:H_2O (1:2) [see Fig. 1b] kept at 1.0 $\pm$ 0.1 °C as to maximize the etch selectivity with InP. The final result is a chip of suspended device coupons ready to be picked up and transfer-printed to the new substrate [see Fig. 1(c)]. The devices were transfer-printed epitaxial side up to Si and SOI substrates, to a Ti : Au (10 nm : 150 nm) coated Si substrate and to a SiO_2 coated Si substrate by exploiting direct van der Waals adhesion (also known as adhesive-less or direct print). Lasers were also printed on Si and AlN substrates by using an intermediate adhesive layer of benzocyclobutene (BCB) with thickness ranging from 50 nm to 1.2 μm. The yield of the transfer-printed device was >90% for both pick up and print.

B. Measurement Setup

The experimental setup used for thermal characterization allowed the extraction of light-current (L-I) and voltage-current (V-I) characteristics in continuous wave (CW) and pulsed wave (PW). Several devices were tested in each experiment to validate that the reported values are representative of a particular

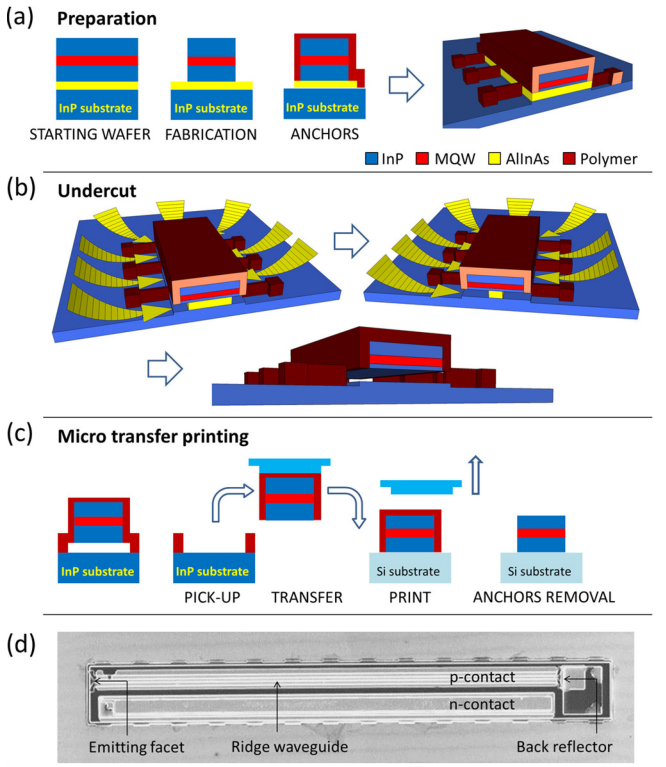

Fig. 1. (a) Cross-section of a laser coupon fabricated on the InP wafer containing the InAlAs sacrificial layer and anchored to the substrate by a resist tether structure. (b) The undercut in $FeCl_3$:H_2O results in suspended coupons ready for micro-transfer-printing. (c) In μTP a PDMS stamp collects the devices from the original wafer and releases them to the target substrate. (d) Scanning electron microscope image of a laser printed on a Si substrate, the main components of the device are indicated.

process. The InP chip and the substrates with the transferred devices were mounted on a copper heat sink with an intermediate layer of thermally conductive paste. The heat sink was in contact with a thermoelectric cooler managed by a temperature controller. The light from the device was collected by a high numerical aperture lens and a 3 mm diameter Ge photodiode or a multimode optical fiber connected to an optical spectrum analyzer (OSA). The OSA allowed monitoring of the individual Fabry-Perot modes and their wavelength shifts due to the temperature dependence of the effective refractive index while varying the temperature of the stage and the electrical power injected into the laser.

III. Laser Characterization

The lasers were characterized electro-optically and thermally on chip (before the undercut) and after transfer-printing to different substrates. The devices show a threshold current I_{th} of 16 mA at room temperature [see Fig. 2a] and series resistance, R_S of 8 Ω. The emitted light power is up to 20 mW at 200 mA depending on the substrate. The free spectral range, $\Delta\lambda$, of the longitudinal modes is measured to be 0.66 nm as expected for a cavity length of 500 μm.

The intrinsic thermal properties of the lasers and the heat sinking properties of the hybrid system were assessed by measurement of the characteristic temperature and thermal impedance of

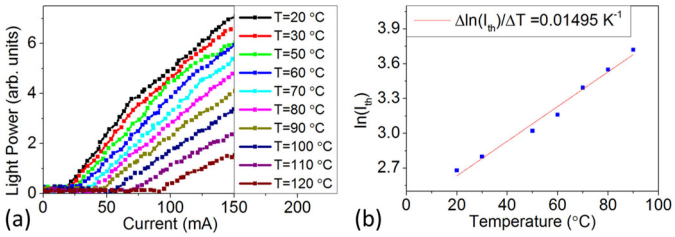

Fig. 2. (a) Pulsed L-Is for stage temperatures between 20–120 °C before μTP, and (b) logarithm of the threshold current against temperature.

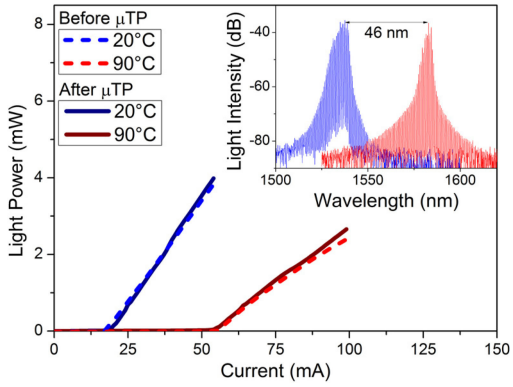

Fig. 3. Comparison of CW – L-Is for etched facet lasers on-chip and printed on Si. The light power before μTP is normalized to those printed on Si as the on-chip light collection is compromised by the adjacent devices. The inset shows the spectra of the laser on chip at 20 °C and 90 °C while operating at 100 mA.

the lasers before and after μTP to different substrates. The analysis of the threshold current at different temperatures permits the extraction of the characteristic temperature, T_0, according to Eq. 1:

$$I_{\rm th} = I_0 e^{T/T_0} \;\Rightarrow\; T_0 = \frac{\Delta T}{\Delta \ln\left(I_{\rm th}\right)} \tag{1}$$

Where, $I_{\rm th}$ is the threshold current, I_0 is a fitting parameter, T is the temperature of the stage and T_0 is the characteristic temperature. High values of T_0 imply that the threshold current density of the device increases less with temperature. III-V laser diodes usually show T_0 in the range 50–100 K. T_0 was calculated from the L-I characteristics before μTP [see Fig. 2(a)] and by applying Eq. 1 in the range of temperatures 20 °C–90 °C [see Fig. 2(b)]. The measurements were performed in pulsed mode with 2% duty cycle and pulse width of 500 ns to ensure limited additional heating. The characteristic temperature of the laser is determined to be $T_0 \sim 67$ K. The redshift of the main emission peak when operating in CW is about 46 nm over 20 °C to 90 °C or 0.65 nm/°C, the corresponding shift in bandgap is about 23 meV [see Fig. 3 inset]. The thermal impedance quantifies the temperature rise of the laser junction for a given input power and thus how efficiently the heat can be removed to the heat sink. The experimental thermal impedance, $Z_{\rm EXP}$, can be determined by comparing the shift in wavelength for an individual longitudinal mode as a function of injected electrical power at room temperature, $\Delta\lambda/\Delta$P, to the wavelength shift of an individual longitudinal mode given by a change in the stage temperature at a constant injected current $\Delta\lambda/\Delta$T [Eq. 2]:

$$Z_{EXP} = \frac{\Delta\lambda}{\Delta P} \Big/ \frac{\Delta\lambda}{\Delta T} \tag{2}$$

$\Delta\lambda/\Delta$T is measured in pulsed mode in order to ensure that there is minimal device heating other than that provided by the temperature controlled stage. Due to the shift of $I_{\rm th}$ at higher temperatures, the measurements are done at a current of 100 mA (well above threshold at room temperature) in order to ensure enough light is emitted by the laser at high temperatures. $\Delta\lambda/\Delta$T is measured to be 0.102 $\pm$ 0.004 nm/K. The $\Delta\lambda/\Delta$P set of measurements are performed in CW. In all the experiments a single longitudinal mode in the laser spectrum is monitored. The experimental thermal impedance, $Z_{\rm EXP}$, of the lasers on-chip and printed on different substrates are reported in Table I. The lasers on the source InP wafer (before μTP) have a measured $Z_{\rm EXP}$ at 57 K/W. Lasers that are printed directly on bare Si show lower values of $Z_{\rm EXP}$ at 38 K/W, in this case the threshold current is similar to the devices on chip indicating there are no negative effects introduced on the device by μTP [see Fig. 3].

The devices printed on a Ti : Au (10 nm : 150 nm) coated Si substrate show the lowest $Z_{\rm EXP}$ of 37 K/W. In particular, the introduction of this layer allows for potential electrical connections through the bottom side of the laser. The thermal impedance of devices printed on an adhesive or thermally insulating intermediate layer such as BCB or SiO_2 increases with the thickness of this layer. Lasers printed on SOI have $Z_{\rm EXP}$ of 94 K/W which is more than twice that of the devices on a 500 μm thick Si substrate. As the substrate material is highly influential on the resulting thermal impedance, some lasers were printed on AlN which is known to have high thermal conductivity with values depending on its preparation method. Here we used a 650 μm thick AlN substrate ($\sigma = 170$ Wm^{-1}K^{-1}) with surface roughness of 30 nm and up to 60 nm high grains that required a 60 nm thick BCB adhesive layer in order to bond the laser to the substrate. In this case, the thermal impedance was still comparable to the devices on chip and measured at $Z_{\rm EXP} =$ 52 K/W. This experiment underlines once again the importance of having highly flat and smooth bonding surfaces in order to obtain adhesive-less printed devices and the best thermal sinking to the substrate [12].

TABLE I
EXPERIMENTAL THERMAL IMPEDANCES OF LASERS ON THE ORIGINAL INP SUBSTRATE AND TRANSFER-PRINTED ON DIFFERENT TARGET SUBSTRATES

Integration Platform	Z_{EXP} (K/W)
On-chip InP (350 μm)	57 ± 4
Bare Si (500 μm)	38 ± 3
Ti : Au (10 : 150) nm	37 ± 2
SiO_2 (50 nm) on Si (500 μm)	43 ± 3
SiO_2 (1 μm) on Si (500 μm)	79 ± 4
SOI (top Si layer 220nm on SiO_2 2 μm)	94 ± 4
BCB (50 nm) on Si (500 μm)	56 ± 4
BCB (1.2μm) on Si (500 μm)	206 ± 9
BCB (60 nm) on AlN (650 μm)	52 ± 3

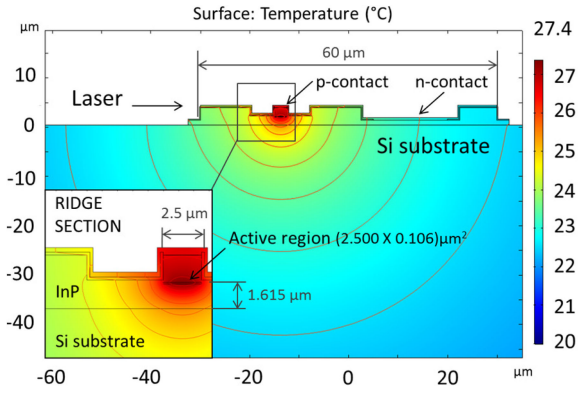

Fig. 4. Cross section of the InP laser printed on a Si substrate (scale 1:1) and the simulated 2D-temperature distribution. $T_{\max} = 27.4$ °C is reached at 100 mA and 2 V bias.

IV. Simulations

The junction temperature, $T_{\max}$, of a laser depends on the amount of heat that is generated, on the location of the heat source, by the heat sink and the ambient temperature. Important parameters in the determination of $T_{\max}$ are the thermal conductivities and the geometry of the surrounding layers (including contact and passivation layers) and components (substrate, submount, etc.). The heat generated by the laser is due to Joule heating associated to the series resistance of the device and by non-radiative processes such as Auger recombination and free carrier absorption which generate heat mainly in the active region or in the adjacent p- cladding layer [31], [32].

Here we consider a 500 μm long active region with cross section of $2.500 \times 0.106\ \mu m^2$ as the source of power dissipation. This region is positioned under the ridge and above the 115 nm thick cladding layer and the 1.5 μm thick n-InP layer as in the real laser. We use $\sigma = 68\ \mathrm{Wm^{-1}K^{-1}}$ for the whole epitaxial structure. If we include the lower thermal conductivity of the active region in the model, the increase in Z_t is simulated to be 0.5 K/W for the laser printed on Si. The model considers a SiO_2 encapsulation layer which insulates the device at the top side making the heat dissipation possible only through the bottom surface, although this is not completely accurate as some heat could spread through the probes used for contacting the devices or in the surrounding air. The heat transfer characteristics of the laser were modeled using COMSOL [33] which uses Fourier's law of heat conduction to calculate the 2D steady state heat flow:

$$q = -\sigma \cdot \nabla T \tag{3}$$

Where q is the heat flux, σ the thermal conductivity tensor and ∇T is the thermal gradient between the heat source and the heat sink. The Finite Element Model (FEM) provides 2-D cross-sectional temperature distributions for the laser on-chip and printed on the diverse platforms. The cross-section and the dimensions of the heterogeneous laser used in the model are illustrated in Fig. 4. They match the geometry of the lasers measured. The thermal conductivity used for modeling the different materials is indicated in Table II.

TABLE II
Thermal Conductivity, σ, of the Materials Used in the Model

Material	σ ($\mathrm{W{\cdot}m^{-1}K^{-1}}$)
InP	68
InAlAs	15
Si	131
Au	318
AlN	170
BCB	0.29
SiO_2	1.4

TABLE III
Comparison of the Experimental, Z_{EXP}, and the Modeled, Z_t, Thermal Impedances for the Lasers Printed Onto Different Platforms

Integration Platform	Z_{EXP} (K/W)	Z_t (K/W)
On-chip InP (350 μm)	57 ± 4	60.5 ± 0.2
InP - no InAlAs (350 μm)	-	57.3 ± 0.2
Bare Si (500 μm)	38 ± 3	38.0 ± 0.2
Ti : Au (10 : 150) nm	37 ± 2	37.5 ± 0.2
AlN (650 μm)	-	32.9 ± 0.2
SiO_2 (50 nm) on Si	43 ± 3	42.7 ± 0.2
SiO_2 (1 μm) on Si	79 ± 4	82.7 ± 0.2
SOI-top (Si 220 nm on SiO_2 2 μm)	94 ± 4	104.8 ± 0.2
SOI-Si substrate (770 μm)	-	40.1 ± 0.2
BCB (50 nm) on Si	56 ± 4	54.0 ± 0.2
BCB (1.2 μm) on Si	206 ± 9	205.7 ± 0.2
BCB (60 nm) on AlN	52 ± 3	52.4 ± 0.2

Each laser configuration is characterized by its theoretical thermal impedance, Z_t, which is approximated by the simplified steady-state analytic expression:

$$Z_t = \frac{\Delta T}{\Delta P} = \frac{T_{\max} - T}{P_{\mathrm{el}} - P_{\mathrm{opt}}} \tag{4}$$

where ΔT is the temperature variation induced by the heating. $T_{\max}$ is the maximum temperature in the device and T is the temperature of the heat sink. ΔP approximates the heat generated in the junction per unit time and is given by subtracting the optical power emitted by the device, P_{opt}, from the total electrical power, P_{el}, injected into the device. P_{el} and P_{opt} are calculated from the experimental V-I and L-I characteristics. P_{el} is much larger than P_{opt} – the best lasers at this wavelength range have wall plug efficiencies $< 30\%$ – and gives the strongest contribution to the determination of the thermal impedance. This highlights why heat management is a significant issue even for the most efficient laser devices. Finally, the simulations provide $T_{\max}$ for each configuration and Eq. (4) allows the calculation of the thermal impedance. Table III compares the simulated and the experimental thermal impedances. All the Z_t values are calculated for the laser operating at 100 mA and for the heat sink temperature at 20 °C. For currents lower than ~50 mA, the simulated ΔP is not linearly dependent on the injected current, due to its calculation from the experimental V-I and L-I curves. In this case Eq. 4 is not reliable for the calculation of Z_t [see Fig. 5].

A 500 μm long laser on the original 350 μm thick InP substrate before undercut has a simulated $T_{\max} = 29.3$ °C when operating at 100 mA. Considering an estimated thermal conductivity of the InAlAs layer, σ(InAlAs)~15

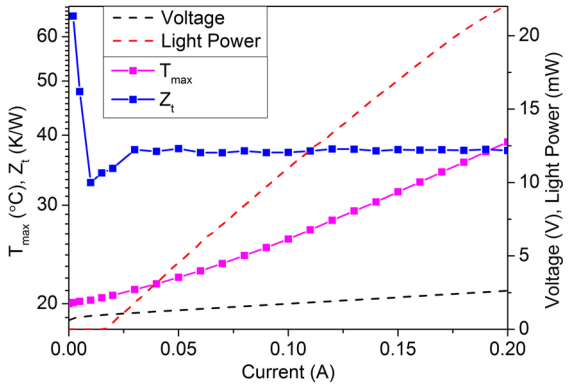

Fig. 5. Experimental L-I and V-I characteristics for the laser printed on Au-coated Si along with the simulated $T_{\max}$ and Z_t. For currents higher than 50 mA, Z_t is within 0.2 K/W of its asymptotic value. The actual device exhibits threshold of ~16 mA, emitted light power >20 mW at 200 mA and a series resistance of 8 Ω.

$Wm^{-1}K^{-1}$ [34], [35], Z_t is calculated to be 60.5 K/W. The same laser without the InAlAs sacrificial layer would have $Z_t = 57.3$ K/W. The thermal impedance for lasers printed directly on a 500 μm thick Si substrate is 38 K/W and is reduced to 37.5 K/W with a Ti : Au (10 nm : 150 nm) intermediate layer. Adhesive-lessly printing the laser to a 650 μm thick AlN substrate (σ(AlN)~170 $Wm^{-1}K^{-1}$) should give $Z_t = 32.9$ K/W if ideal bonding can be achieved. With a 60 nm BCB adhesive layer Z_t rises to 52.4 K/W.

If a 50 nm or 1 μm thick SiO_2 layer is interposed between the device and a Si substrate the simulated thermal impedance is respectively 42.7 K/W and 82.7 K/W. In particular, a laser printed on the 220 nm thick Si waveguiding layer on top of a 2 μm buried oxide and a 770 μm Si substrate (SOI) would have $Z_t = 104.8$ K/W. The same laser printed directly on the 770 μm thick Si substrate of the SOI would have a reduced thermal impedance of 40.1 K/W. In the case where a 50 nm or a 1.2 μm thick adhesive BCB layers is used to bond a laser to a 500 μm thick Si substrate, Z_t is expected to be 54.0 K/W and 205.7 K/W respectively. The simulation results are within 10% of our experimental results. Differences between experiment and model can be ascribed to less-than-optimum adhesion to the substrate given by interface roughness or to a difference in layer thicknesses. Heat spreading through the metal probes can also become significant, especially for situations with high thermal impedance to the substrate. Changes in the geometry of the hybrid system have been investigated in order to understand their effects on the thermal impedance. Lasers transfer-printed to highly thermally conductive substrates such as Si or AlN offer superior thermal impedance compared to those on the native InP [see Fig. 6(a)]. Consequently, a lower limit for the thermal impedance of a heterogeneously integrated laser is set by the substrate, in particular by its thermal conductivity and only partially by its thickness (usually >350 μm). The variation of Z_t with the thickness of diverse intermediate layers between the Si substrate and the devices is reported in Fig. 6(b). Thick, highly thermally conductive intermediate layers only slightly enhance the thermal sink properties of the system while insulating layers reduce the heat sinking as their thicknesses increases. In particular, the simulation shows how a BCB layer thinner than 50 nm would reduce the Z_t of the integrated device. The lasers printed on top of an SOI wafer have shown more than twice the thermal impedance of those printed directly on the Si substrate. As shown in Fig. 6(c), the cross-sectional temperature profile of the SOI indicates that the heat tends to spread sideways and preferentially along the Si waveguiding layer potentially affecting other elements on the integration platform located at up to 100 μm far from the ridge. This is due to the insulating properties of the buried oxide. This issue could be addressed by defining thermally insulating trenches around the laser in order to channel the heat downwards but this would lead to a few K/W increase in Z_t. Moreover, the arrangement of such trenches at the front and the back facet can be difficult especially if the SOI waveguide lies under the device as in the case of evanescently coupled devices. Printing the laser source directly on the substrate of the SOI offers a lower Z_t with another advantage being due to the thermal insulating properties of the buried oxide which prevents the heat to reflow up towards the Si waveguiding layer and the other components on it. In the case of adhesive-less printing, Z_t decreases by a few K/W if the active region is closer than 3 μm to the substrate by thinning the n-InP layer. For standard edge coupled laser designs the thickness of this layer must be greater than 1.5 μm in order to avoid any modal interaction with the Si substrate [10], [12]. On the other hand, if a thermally insulating layer is interposed between the printed device and the substrate then a thicker n-InP layer lowers the heat density in the device reducing $T_{\max}$ and then Z_t [see Fig. 6(d)].

Scaling analysis keeping the injection current constant shows that Z_t decreases inversely to the cavity length since the heat generation per unit area is correspondingly lower [see Fig. 7(a)]. In the case the current density is kept constant while varying the cavity length, the Z_t variation with the cavity length is even stronger. Z_t variations with the cavity length are reduced for lasers longer than 1 mm in both cases. A 1 mm device shows a simulated thermal impedance of 18.6 K/W. If the lasers are printed on an intermediate or adhesive insulating layer the variation in Z_t with cavity length is stronger, especially for cavity lengths <1 mm [see Fig. 7(b)]. More generally, the thermal impedance of longer devices is less affected by the material and the thickness of the intermediate layer. While Z_t is lower for longer devices the absolute heat generated and the electrical power injected in a long laser may be higher than for shorter lasers due to the reduced slope efficiency of longer devices. It is important to find the right balance between the total heat produced by the device, the electrical power and the cavity length according with the final application. Changes in the laser coupon width were studied for lasers with the ridge in the center of the coupon and no n-contact recess [Fig. 7(c) inset]. Adhesive-lessly printed coupons wider than 60 μm exhibit a reduction of Z_t <1 K/W [see Fig. 7(c)]. Reduction in Z_t with the width of the coupon is more evident for devices printed on thick insulating layers like SiO_2 or BCB [see Fig. 7(d)]. For a laser with electrical contacts on the top side, the distance of the n-contact recess to the active ridge only marginally affects

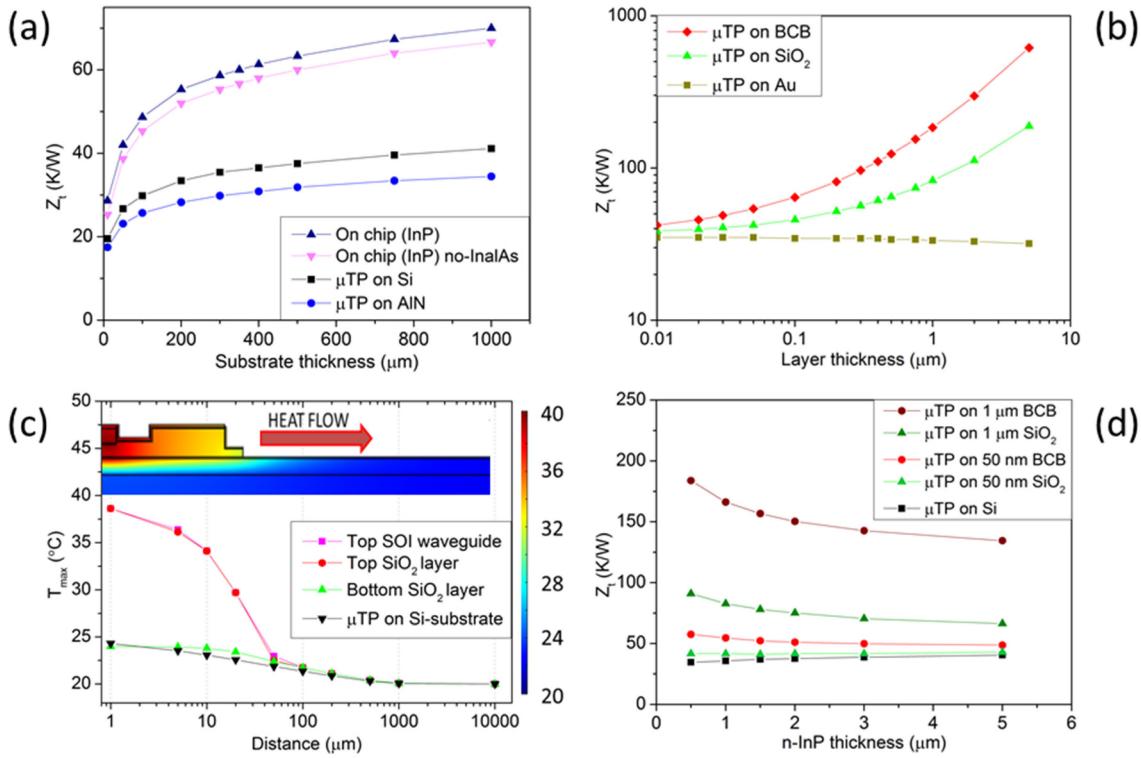

Fig. 6. (a) Variation in Z_t with the substrate thickness for lasers on-chip and adhesive-lessly printed onto Si and AlN substrates. (b) Z_t dependence on the thickness of Au, SiO_2 or BCB layers interposed between the device and a 500 μm thick Si substrate. (c) Temperature profile along the different layers of the SOI when the laser is in operation. The inset shows a 2D-temperature profile (using the log-scale for distance) graphically illustrating the lateral heat spreading. (d) Z_t dependence on the thickness of the n-InP layer for different substrate configurations.

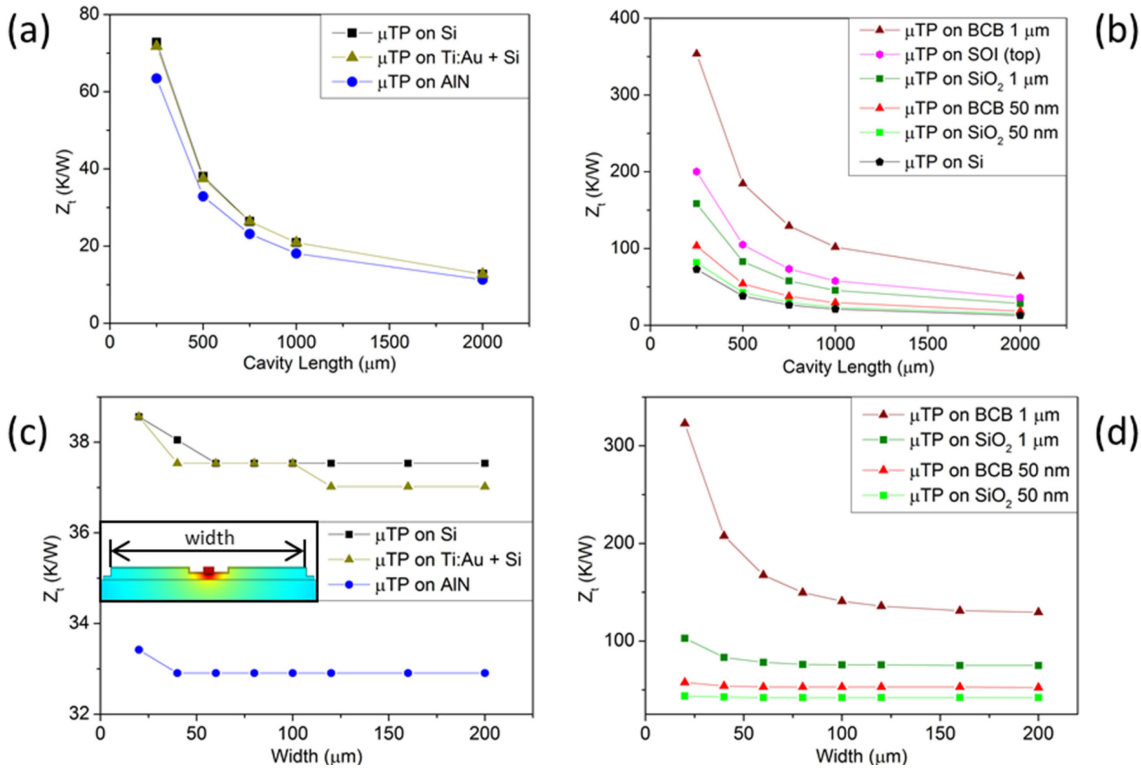

Fig. 7. (a) Z_t dependence on cavity length for devices printed on highly thermally conductive substrates and (b) on thermally insulating interface layers. (c) Z_t versus width for coupons adhesive-lessly printed on highly thermally conductive substrates and (d) with thermally insulating interface layers.

the thermal impedance of devices adhesive-less printed on Si or AlN, but can have an effect as large as a few K/W on devices printed on thermally insulating layers because of the higher lateral heat spreading. Increased thickness of the p-contact metal and reduced thickness of the dielectric layer used for passivation of the coupon can potentially reduce Z_t further. In order to estimate such reduction, the heat exchange to the surrounding air must be included in the model [22]. Use of metallic thermal vias from the top of the devices to the underlying substrate is also an option for reducing Z_t of devices printed on the thermally insulating layers.

V. Conclusions

Our 500 μm long etched-facet transferable ridge lasers have shown threshold current of $\sim$16 mA, high light power and T_0 of 67 K. The lasers have a measured thermal impedance of 38 K/W when transfer-printed directly on silicon which is a 30% improvement compared to those on-chip. The 2D-FEM thermal model predicts Z_t which is within 10% of the experimental results. The model indicates that BCB adhesive layers should be as thin as possible in order to achieve best thermal sinking through the substrate. Thicker adhesive layers should be carefully evaluated when a III-V laser needs to be incorporated onto SOI, especially for short device lengths. Lasers transfer-printed on the silicon substrate of a SOI wafer (Z_t $\sim$40 K/W) result in more than two times lower Z_t than those printed on the SOI side where Z_t is $\sim$105 K/W. This integration approach allowed by μTP could lead to conspicuous power savings and reduced influence of the active devices on the other elements in silicon photonics integrated circuits especially when the platform hosts a great amount of integrated devices close to each other.

References

[1] D. Thomson *et al.*, "Roadmap on silicon photonics," *J. Opt.*, vol. 18, 2016, Paper no. 073003.

[2] D. Liang and J. E. Bowers, "Recent progress in lasers on silicon," *Nature Photon.*, vol. 4, pp. 511–517, 2010.

[3] G. Roelkens *et al.*, "III-V/silicon photonics for on-chip and intra-chip optical interconnects," *Laser Photon. Rev.*, vol. 4, pp. 1–29, 2010.

[4] B. Song, C. Stagarescu, S. Ristic, A. Behfar, and J. Klamkin, "3D integrated hybrid silicon laser," *Opt. Express*, vol. 24, no. 10, pp. 10435–10444, 2016.

[5] A. W. Fang, H. Park, O. Cohen, R. Jones, M. J. Paniccia, and J. E. Bowers, "Electrically pumped hybrid AlGaInAs-silicon evanescent laser," *Opt. Express*, vol. 14, no. 20, pp. 9203–9210, 2006.

[6] M. Lamponi *et al.*, "Low-threshold heterogeneously integrated InP/SOI laser with a double adiabatic taper coupler," *IEEE Photon. Technol. Lett.*, vol. 24, no. 1, pp. 76–78, Jan. 2012.

[7] B. Ben Bakir *et al.*, "Electrically driven hybrid Si/III-V lasers based on adiabatic mode transformers," *Opt. Express*, vol. 19, no. 11, pp. 10317–10325, 2011.

[8] A. W. Fang *et al.*, "Integrated AlGaInAs-silicon evanescent race track laser and photodetector," *Opt. Express*, vol. 5, pp. 2315–2322, 2007.

[9] B. Corbett, R. Loi, W. Zhou, D. Liu, and Z. Ma, "Transfer print techniques for heterogeneous integration of photonic components," *Prog. Quantum Electron.*, vol. 52, pp. 1–17, 2017.

[10] J. Justice, C. Bower, M. Meitl, M. B. Mooney, M. A. Gubbins, and B. Corbett, "Wafer-scale integration of group III-V lasers on silicon using transfer printing of epitaxial layers," *Nature Photon.*, vol. 6, no. 9, pp. 610–614, 2012.

[11] H. Yang *et al.*, "Transfer printing stacked nanomembrane lasers on silicon," *Nature Photon.*, vol. 6, pp. 617–622, 2012.

[12] R. Loi *et al.*, "Transfer printing of AlGaInAs/InP etched facet lasers to Si substrates," *IEEE Photon. J.*, vol. 8, no. 6, Dec. 2016, Paper no. 1504810.

[13] J. Zhang *et al.*, "Transfer-printing-based integration of a III-V-on-silicon distributed feedback laser," *Opt. Express*, vol. 26, pp. 8821–8830, 2018.

[14] A. De Groote *et al.*, "Transfer-printing based integration of single-mode waveguide-coupled III-V-on-silicon broadband light emitters," *Opt. Express*, vol. 24, pp. 13754–13762, 2016.

[15] L. Liu *et al.*, "On-chip optical interconnect on silicon by transfer printing," in *Proc. Conf. Lasers Electro-Opt.*, 2018, Paper no. STh4B.1.

[16] D. Gomez *et al.*, "Process capability and elastomer stamp lifetime in micro transfer printing," in *Proc. 2016 IEEE 66th Electron. Compon. Technol. Conf.*, Las Vegas, NV, USA, 2016, pp. 680–687.

[17] J. Yoon, S. M. Lee, D. Kang, M. A. Meitl, C. A. Bower, and J. Rogers, "Heterogeneously integrated optoelectronic devices enabled by micro-transfer printing," *Adv. Opt. Mater.*, vol. 3, no. 10, pp. 1313–1335, 2015.

[18] A. Carlson, A. M. Bowen, Y. Huang, R. G. Nuzzo, and J. A. Rogers, "Transfer printing techniques for materials assembly and micro/nanodevice fabrication," *Adv. Mater.*, vol. 24, pp. 5284–5318, 2012.

[19] M. A. Meitl *et al.*, "Transfer printing by kinetic control of adhesion to an elastomeric stamp," *Nature Mater.*, vol. 5, pp. 33–38, 2006.

[20] C. A. Bower *et al.*, "Emissive displays with transfer-printed assemblies of 8 μm $\times$ 15 μm inorganic light-emitting diodes," *Photon. Res.*, vol. 5, no. 2, pp. A23–A29, 2017.

[21] C. Chen, T. Zhang, P. Contu, J. Klamkin, A. K. Coskun, and A. Joshi, "Sharing and placement of on-chip laser sources in silicon-photonic noCs," in *Proc. 8th IEEE/ACM Int. Symp. Netw. Chip*, 2014, pp. 88–95.

[22] Z. H. Quan, J. Justice, M. B. Mooney, M. A. Gubbins, P. J. Parbrook, and B. Corbett, "Thermal modelling of transfer-bonded thin-film gallium arsenide laser diode," *IET Optoelectron.*, vol. 10, pp. 51–56, 2016.

[23] M. Sysak *et al.*, "Experimental and theoretical thermal analysis of a hybrid silicon evanescent laser," *Opt. Express*, vol. 15, pp. 15041–15046, 2007.

[24] M. N. Sysak *et al.*, "Hybrid silicon laser technology: A thermal perspective," *IEEE J. Sel. Topics Quantum Electron.*, vol. 17, no. 6, pp. 1490–1498, Nov./Dec. 2011.

[25] S. Cheung, Y. Kawakita, K. Shang, and S. J. B. Yoo, "Theory and design optimization of energy-efficient hydrophobic wafer-bonded III-V/Si hybrid semiconductor optical amplifiers," *J. Lightw. Technol.*, vol. 31, no. 24, pp. 4057–4066, Dec. 2013.

[26] G. Roelkens *et al.*, "III-V/Si photonics by die-to-wafer bonding," *Mater. Today*, vol. 10, nos. 7/8, pp. 36–43, 2007.

[27] B. Song, L. Megalini, S. Dwivedi, S. Ristic, and J. Klamkin, "High-thermal performance 3D hybrid silicon lasers," *IEEE Photon. Technol. Lett.*, vol. 29, no. 14, pp. 1143–1146, Jul. 2017.

[28] R. Loi *et al.*, "Micro-transfer printing for advanced scalable hybrid photonic integration," in *Proc. Eur. Conf. Integr. Opt.*, 2018, Paper no. Th.1.A.5 15.

[29] J. Juvert *et al.*, "Integration of etched facet, electrically pumped, C-band Fabry-Pérot lasers on a silicon photonic integrated circuit by transfer printing," *Opt. Express*, vol. 26, pp. 21443–21454, 2018.

[30] J. O'Callaghan *et al.*, "Comparison of InGaAs and InAlAs sacrificial layers for release of InP-based devices," *Opt. Mater. Express*, vol. 7, pp. 4408–4414, 2017.

[31] J. Piprek, J. Patrick, A. Patrick, and J. E. Bowers, "Carrier non-uniformity effects on the internal efficiency of multiquantum-well lasers," *Appl. Phys. Lett.*, vol. 74, no. 4, pp. 489–49, 1999.

[32] J. Piprek, J. K. White, and A. J. SpringThorpe, "What limits the maximum output power of long-wavelength AlGaInAs/InP laser diodes?," *IEEE J. Quantum Electron.*, vol. 38, no. 9, pp. 1253–1259, Sep. 2002.

[33] *COMSOL V4.0 Heat Transfer Theory*, COMSOL, Burlington, MA, USA, 2010.

[34] S. Adachi, "Lattice thermal resistivity of III–V compound alloys," *J. Appl. Phys.*, vol. 54, no. 4, pp. 1844–1848, 1983.

[35] S. Adachi, "Lattice thermal conductivity of group-IV and III–V semiconductor alloys," *J. Appl. Phys.*, vol. 102, no. 6, 2007, Paper no. 063502.

Authors' biographies not available at the time of publication.